ChemPlusChem

Research Article
doi.org/10.1002/cplu.202500376

Chemistry Europe
European Chemical Societies Publishing

www.chempluschem.org

Solid Porous Materials for Selective Capture and Separation of Sulfur Hexafluoride (SF_6)

Julio E. Sosa, Rui P. P. L. Ribeiro, Srdana Kolakovic, Inês Matos, Maria Bernardo, José P. B. Mota, João M. M. Araújo, and Ana B. Pereiro*

Developing technologies to capture, purify, and reuse potent greenhouse gases such as sulfur hexafluoride (SF_6) is crucial because of their high global warming potential. Porous solid matrices are promising candidates for this purpose, due to their high surface areas and pore volumes. Herein, two coconut shell–derived activated carbons (AC) (CS-CO_2 and CS-$ZnCl_2$), obtained through physical and chemical activation, are evaluated and compared with two commercial adsorbents: an AC monolith (ACM) and a metal-organic framework. The adsorption capacities for SF_6 and nitrogen (N_2) are measured gravimetrically at three temperatures: 283.15, 303.15, and 323.15 K. The experimental data are fitted using the Toth model, and the impact of temperature and pressure on the adsorption performance is analyzed. The order of SF_6 adsorption capacity is: ACM > CS-$ZnCl_2$ > Fe-BTC > CS-CO_2, reflecting dependence on surface area. Selectivity for SF_6/N_2 separation is evaluated using Ideal Adsorbed Solution Theory, with ACM exhibiting the highest adsorption capacity due to its selective separation properties. These findings contribute to the understanding and selection of efficient adsorbent materials for SF_6 separation and recovery, providing valuable insights for their future implementation in industrial gas treatment and environmental management applications.

1. Introduction

The impacts of climate change and global warming are increasingly evident across both developed and developing countries, manifesting through intensified precipitation patterns, rising sea levels, and elevated global temperatures that are becoming major concerns.[1–4] These phenomena are closely linked to the emission of greenhouse gases (GHGs), including fluorinated gases (F-gases), which account for ≈2.6% of total GHG emissions.[5,6] Among them, sulfur hexafluoride (SF_6) stands out as a particularly potent climate forcer, with a global warming potential ≈22,800 times higher than that of carbon dioxide (CO_2).[6] Its exceptional atmospheric persistence and strong radiative efficiency have made it one of the GHGs regulated under the Kyoto Protocol, highlighting the urgent need for advanced capture and recovery strategies.[7] In the U.S.A., the EPA has identified SF_6 as a gas that poses a serious threat to public health and the environment[8,9] primarily due to its extremely high global warming potential and potential health impacts. High levels of this gas may lead to adverse effects such as hepatic and renal damage, along with respiratory impairment that can progress to pulmonary edema, a life-threatening condition.[10–13]

One of the main sources of SF_6 emissions is the improper handling and inadequate maintenance of equipment containing the gas, resulting in significant leaks and subsequent atmospheric release.[9,14] ≈80% of SF_6 is used in the energy sector as a dielectric gas in electrical equipment, while about 4–8% is employed in the magnesium industry and in semiconductor manufacturing.[8,10,15] In these applications, SF_6 is employed as a cover gas at concentrations of 0.2–3%, resulting in direct atmospheric emissions during molten magnesium protection and during semiconductor etching and cleaning processes.[15,16] Consequently, energy-efficient separation technologies capable of directly recovering high-purity SF_6 are urgently required to ensure its sustainable use throughout the life cycle.[15,17,18] Due to its high cost and environmental impact, SF_6 is often used in diluted mixtures with inert gases such as nitrogen (N_2), minimizing its direct release into the atmosphere.[9,19,20] Furthermore, studies have reported that in SF_6/N_2 mixtures with proportions of 0.1–2.4% SF_6, degradation efficiencies of up to 0.99% can be achieved,[8,21–24] providing a promising technological pathway to mitigate its environmental impact.[8,21–24] In this work, the concentration $SF_6/N_2 = 0.02/0.98$ (v/v) mixture was selected based on its industrial relevance, since SF_6 is widely used in electrical

J. E. Sosa, S. Kolakovic, I. Matos, M. Bernardo, J. P. B. Mota, J. M. M. Araújo, A. B. Pereiro
LAQV
REQUIMTE
Department of Chemistry
NOVA School and Technology
NOVA University Lisbon
Caparica 2829–516, Portugal
E-mail: anab@fct.unl.pt

R. P. P. L. Ribeiro
Green Hydrogen Collaborative Laboratory
Estrada Nacional 120–1 Central Thermoelectrical
Sines 7520–089, Portugal

Supporting information for this article is available on the WWW under https://doi.org/10.1002/cplu.202500376

equipment, semiconductor manufacturing, and magnesium smelting. In these industrial processes, residual gases contain moisture due to prior treatment with alkaline aqueous solutions to remove acidic impurities.[17] The presence of water can affect the adsorption and selectivity of these gases in porous solid matrices by competing for active sites or even blocking them.[25,26] However, before being used for separation and purification, these gases must be characterized,[27] and a pretreatment must also be applied to remove particles and humidity. In summary, the separation of SF_6/N_2 mixtures has become a focal point of research, with porous materials—including metal-organic frameworks (MOFs), activated carbons (ACs), zeolites, and mesoporous silicas—being widely investigated for their potential in selective adsorption and gas recovery applications.[7,17,19,28–42]

MOF materials have attracted significant attention for SF_6 separation due to their tailorable pore structures and high surface areas. In particular, M-MOF-74 (M = Mg, Co, Zn) has demonstrated a strong affinity for SF_6, attributed to favorable host-guest interactions that enhance selective adsorption.[28] Pore size also plays a crucial role in performance: small-pore MOFs enhance selective separation, while large-pore MOFs are generally more effective for SF_6 storage due to their higher capacity.[29] Comparative studies on UIO-66 and UIO-67 reveal that UIO-67 offers superior selectivity, likely due to more optimal pore packing for SF_6 molecules.[43] Additionally, Sc-cage-MOF and YTU-30 have shown enhanced SF_6 adsorption through specific interactions.[37,44] Other MOFs, such as SNNU-202, SNNU-203, and SNNU-204, exploit binuclear metal sites and aromatic rings to strengthen SF_6 adsorption via synergistic interactions.[38] Additionally, Beijing University of Technology (BUT)-53 has demonstrated the ability to recover high-purity SF_6 (>99.9%) even under humid conditions, proving to be a promising approach for sustainable SF_6 capture.[17] Furthermore, GNU-3, a cobalt-based MOF with nanomolecular traps and well-defined pores, efficiently captures SF_6 from N_2 mixtures due to strong supramolecular interactions, exhibiting high selectivity and excellent regeneration capacity.[40] Despite these promising results, the practical deployment of MOFs at an industrial scale is hindered by their often complex and costly synthesis, which remains a key barrier to widespread application.

The activation process used in the production of AC is crucial in enhancing its structural and textural properties.[36] Selecting appropriate activation methods can significantly increase surface area and microporosity, while also creating larger mesopores that enhance adsorption capacity for gases such as SF_6.[36] To ensure economic viability, choosing low-cost, sustainable biomass precursors is essential for the development of bio-based ACs (Bio-ACs), aligning with the principles of the circular economy. In this context, coconut shell (CS) waste has emerged as a promising and cost-effective feedstock for Bio-AC production, offering favorable characteristics for industrial-scale gas adsorption applications.

The objective of this study is to evaluate the SF_6 adsorption performance of two BIO-ACs derived from residual coconut shell biomass, prepared via chemical ($ZnCl_2$) and physical (CO_2) activation agents. Physical activation promoted microporosity in the CS-CO_2 material, whereas chemical activation enhanced both micro-/mesoporosity in the CS-$ZnCl_2$. For comparative purposes, two additional materials were included: a commercial AC monolith (ACM) and an MOF (Fe-BTC). These were selected to assess the effectiveness of the BIO-ACs in separating SF_6/N_2 mixtures. Adsorption equilibria for SF_6 and N_2 were measured on all four materials at 283.15, 303.15, and 323.15 K, and the data were fitted using the Toth model. Working capacities were assessed to elucidate the influence of pressure and temperature on separation efficiency. Competitive selectivity for the SF_6/N_2 mixture was evaluated using Ideal Adsorbed Solution Theory (IAST). Additionally, the performance of materials was compared with literature data under conditions of 303.15 K and 0.1 MPa, considering parameters such as selectivity, surface area, and pore volume in relation to SF_6 adsorption. Finally, selection criteria such as Yang's and Ackley's figures of merit (FOM), which incorporate working capacity, selectivity, and regeneration capacity, were applied to both our materials and those reported in the literature to evaluate their potential for industrial applications. Overall, this work provides a significant contribution to advancing SF_6/N_2 separation and offers valuable insights for developing more efficient separation processes.

2. Results and Discussion

2.1. Adsorption Equilibrium of SF_6 and N_2

Table 1 provides the characterizations of the materials studied in this work: surface area, pore size distribution (calculated using the NLDFT model), and pore volume. This characterization was obtained using N_2 adsorption isotherms at 77 K, and the data were published in a previous work.[45] This table presents the surface area of the four porous solid matrices studied, which follow the trend: ACM > CS-$ZnCl_2$ > Fe-BTC > CS-CO_2. This order correlates with the adsorption capacity of SF_6 at pressures below 1.5 MPa (see **Figure 1a**), which is controlled by both the pore size distributions of the materials and the stronger interactions with this F-gas. SF_6 has a diameter of ~ 5.15 Å and a polarizability of 4.49 $Å^3$,[46–48] whereas N_2 has a smaller diameter of ~ 3.64 Å and a lower polarizability of 1.710 $Å^3$.[46–48] These differences significantly influence their interactions with the pore surfaces. Then, SF_6 experiences stronger interactions with the material surfaces due to its higher polarizability and larger size, which explains the adsorption capacity trend. CS-$ZnCl_2$ has a broader

Table 1. Textural parameters of materials studied in this work obtained from N_2 adsorption–desorption isotherms.

Carbon sample	Parameter				Ref.
	S_{BET} [$m^2 g^{-1}$]	v_{total} [$cm^3 g^{-1}$]	v_{micro} [$cm^3 g^{-1}$]	v_{meso} [$cm^3 g^{-1}$]	
CS-CO_2	602	0.245	0.211	0.034	[73]
CS-$ZnCl_2$	1391	0.859	0.240	0.619	
ACM	1446	0.779	0.692	0.088	
Fe-BTC	1213	0.625	0.487	0.139	

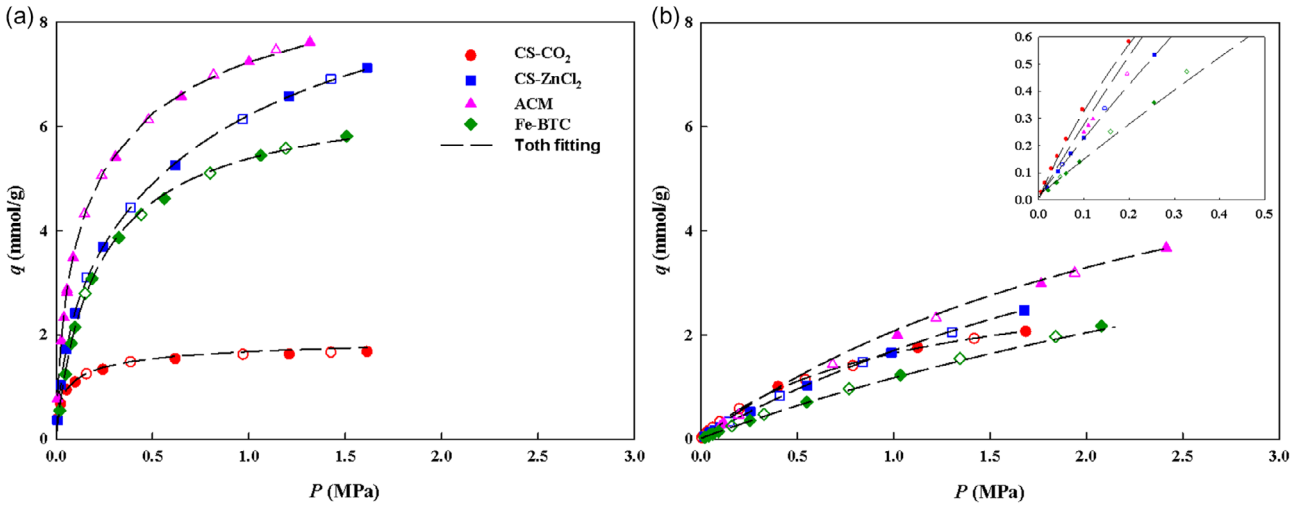

Figure 1. Adsorption (full symbols) and desorption (empty symbols) equilibrium isotherms on: a) SF_6 and b) N_2 at 303.15 K.

micro/mesoporosity of 5–60 Å, including both wide and narrow pores (≤25 Å),[45] allowing more efficient accommodation of SF_6. In contrast, CS-CO_2 exhibits high microporosity with narrow pores mainly in the 5–15 Å range,[45] which restricts the accessibility of the larger and more polarizable SF_6 molecules. ACM and Fe-BTC display intermediate micro/mesoporosity distributions of 5–40 Å and 5–30 Å,[45] respectively. Therefore, the observed surface area ranking reflects not only the textural properties of the materials but also the suitability of their pores for interacting with SF_6, explaining the highest uptake capacity of ACM. N_2 is a smaller-sized and lower polarizability molecule. Then, N_2 adsorption is influenced by micropore accessibility, as demonstrated in Figure 1b. However, the mesopore volume plays a more dominant role, which accounts for the deviations in adsorption trends observed with this gas.

The adsorption equilibria of SF_6 and N_2 on these materials at 283.15, 303.15, and 323.15 K are detailed in Figure 1 and the Supporting Information (see Figure S1–S2 and Table S1–S2, Supporting Information). The experimental data were fitted using the Toth adsorption model, with the corresponding parameters and fitting errors summarized in Table S3, Supporting Information. These results further support the relationship between textural properties and adsorption behavior for both gases. The adsorption trend observed for SF_6 is not mirrored in the case of N_2. At pressures below 0.5 MPa, the order of N_2 adsorption capacity is CS-CO_2 > ACM > CS-$ZnCl_2$ > Fe-BTC (Figure 1b). This sequence does not fully align with the structural characteristics of the materials, primarily due to the deviation of Fe-BTC. One plausible explanation is that the nitrogen molecule, possessing a zero dipole moment, has limited interaction with the Fe (III) active site present in Fe-BTC.[49] When Fe-BTC is excluded, the trend among the remaining materials, CS-CO_2 > ACM > CS-$ZnCl_2$, can be attributed to the increasing mesopore volume, as shown in Table 1. However, at higher pressures ($p > 1$ MPa), the order of adsorption capacity shifts to ACM > CS-$ZnCl_2$ > CS-CO_2 > Fe-BTC. Again, Fe-BTC fails to follow the expected trend based on its structural characteristics, as observed by the other materials. When Fe-BTC is excluded, the adsorption behavior of the other materials corresponds to a decreasing order in surface area and micropore volume, as detailed in Table 1. These results highlight the complex interplay between pore structure, surface area, and the nature of the adsorbate in determining adsorption performance.

The adsorption equilibria are accompanied by desorption, indicating that they do not exhibit hysteresis and that the interactions between adsorbents and adsorbates are purely physical. Such behavior is advantageous for practical separation processes involving multiple adsorption–desorption cycles, as it allows for complete regeneration of the porous materials at room temperature without leaving undesirable residues. To assess the practical applicability of the materials, the working capacity was evaluated as a function of the desorption temperature T_H (ranging from 313.15 to 373.15 K) at a desorption pressure of 0.010 MPa and a feed temperature T_L of 303.15 K.[50,51] This pressure reflects the partial pressure of the commercial SF_6/N_2 mixture (with molar fractions $y_{SF6} = 0.02$ and $y_{N2} = 0.98$) commonly used in the electrical industry.[13] As shown in **Figure 2**, ACM material outperforms the other materials in both SF_6 adsorption at low temperatures and higher working capacity $\Delta_q = \boldsymbol{q}_{T_L} - \boldsymbol{q}_{T_H}$ across the evaluated regeneration temperature range. For instance, at a regeneration temperature of 313.15 K, the working capacity follows the order: ACM (0.60 mmol g^{-1}) > CS-$ZnCl_2$ (0.34 mmol g^{-1}) > CS-CO_2 (0.23 mmol g^{-1}) > Fe-BTC (0.22 mmol g^{-1}). This trend remains consistent at higher regeneration temperatures. Although all materials show promising adsorption–regeneration performance, Fe-BTC consistently exhibits the lowest S_{F6} adsorption capacity. This limitation is attributed to its structural characteristics, such as lower porosity and less favorable distribution of adsorption sites, which hinder its performance in SF_6/N_2 separation under the studied conditions.

In the gas separation process, the effects of the feed pressure and desorption temperature are key parameters influencing adsorption performance. To explore this, the feed pressure varied between 0.1 and 1 MPa, and the T_H ranged from 303.15 to 373.15 K.

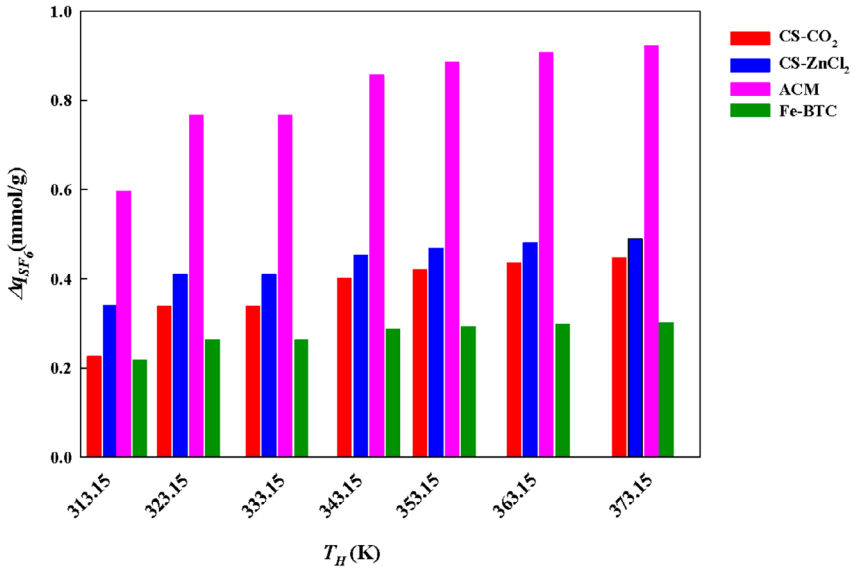

Figure 2. SF_6 working capacity (Δq_{SF_6}) as a function of desorption temperature T_H for isobaric operation at the pressure of 0.010 MPa and temperature of 303.15 K.

Figure 3 presents contour plots illustrating the impact of pressure on the amount of SF_6 absorbed by the materials. For instance, at a desorption temperature of 373.15 K and a feed pressure of $P_{SF6,\ feed} = 0.1$ MPa, the working capacity follows the order: ACM (3.92 mmol g^{-1}) > CS-$ZnCl_2$ (2.56 mmol g^{-1}) > Fe-BTC (2.39 mmol g^{-1}) > CS-CO_2 (1.12 mmol g^{-1}). Increasing the feed pressure to 0.5 MPa at the same desorption temperature results in higher working capacities: ACM (6.46 mmol g^{-1}) > CS-$ZnCl_2$ (5.14 mmol g^{-1}) > Fe-BTC (4.82 mmol g^{-1}) > CS-CO_2 (1.52 mmol g^{-1}). Although the absolute uptake increases with pressure, the ranking of materials remains unchanged. This consistent trend correlates with the surface area of the materials, which decreases in the same order. A larger surface area facilitates the adsorption of a greater number of gas molecules, thereby enhancing performance. These findings confirm that the porous solid matrices studied here are promising candidates for SF_6 separation processes, particularly under controlled pressure and temperature conditions.

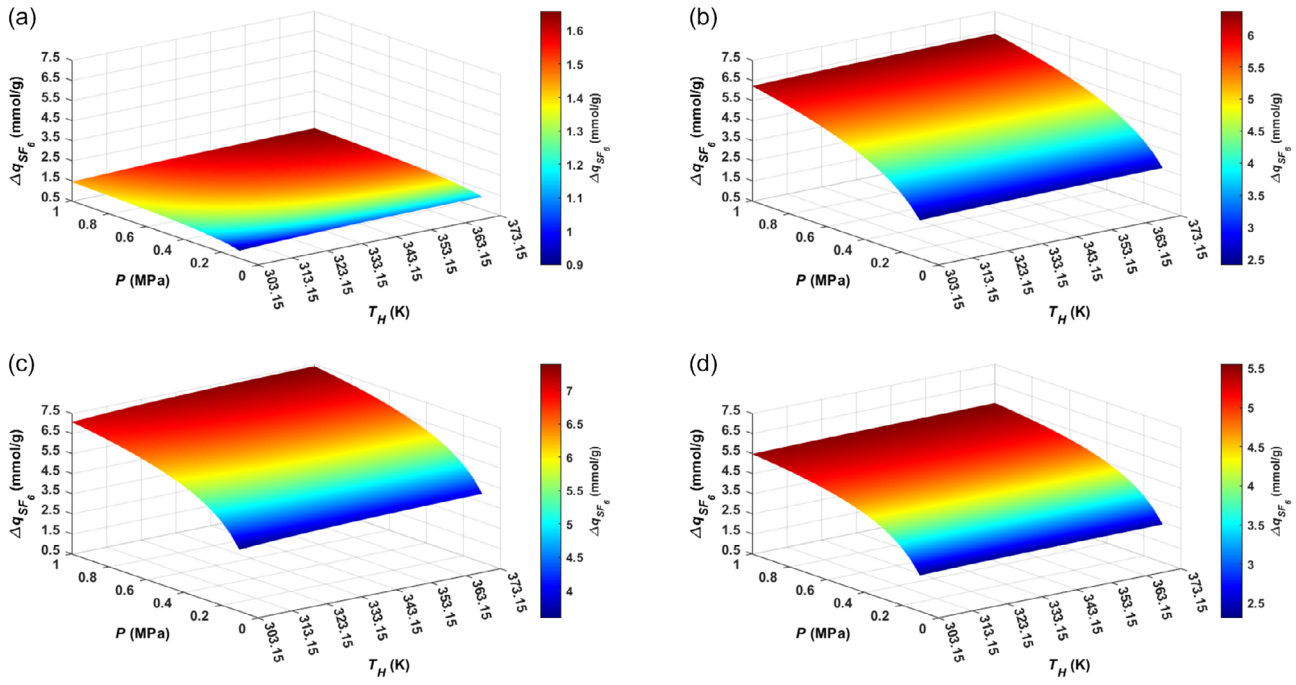

Figure 3. Contour plots of the working capacity (mmol g^{-1}) as a function of the degassing temperature, T_H, and the feed pressure, P on: a) CS-CO_2, b) CS-$ZnCl_2$, c) ACM, and d) Fe-BTC.

2.2. Isosteric Heat of Adsorption and Henry's Law Constant

In the design of gas separation processes, the isosteric heat of adsorption Q_{st} is a key parameter, as it accounts for ≈30% of the total electrical energy consumed during the degassing process.[52,53] As such, Q_{st} is a critical variable for evaluating adsorption efficiency. It serves as an indicator of the strength of interactions between the adsorbent and adsorbate, and it is directly relevant to applications in gas separation, capture, and storage.[52,54–56] In this study, Q_{st} was determined from the experimental adsorption data using the Clausius-Clapeyron equation, according to established methodologies[54,55,57,58]

$$(\log_e P)_q = \text{constant} - \frac{Q_{st}}{RT} \quad (1)$$

where R is the universal gas constant, P is the equilibrium pressure, and T is the temperature.

The experimental adsorption equilibria were fitted using a virial model and subsequently converted to the linear isosteric plots of $(\log_e P)_{q=\text{const}}$ *versus* $1/T$ for different q values: 0.1, 0.45, 0.65, 0.85…n mmol g^{-1}, corresponding to the maximum adsorption loading of each material (see Figure S3–S4, Supporting Information). The isosteric heat of adsorption (Q_{st}) for SF_6 across all porous solid matrices lies within the theoretical range of 25–35 kJ mol^{-1} (see **Figure 4a**).[54,59] For a consistent comparison across all materials, the analysis was limited to adsorption capacities up to 2 mol·kg^{-1}, corresponding to the maximum adsorption loading of CS-CO_2, the material with the lowest adsorption capacity. Within this range, Q_{st} remains relatively uniform and linear, reflecting the consistent energetic interactions across the adsorbents. N_2 does not follow the same SF_6 trend, mainly due to its much lower polarizability (1.710 $Å^3$) and its smaller diameter (≈3.64 Å).[46–48] These properties lead to weaker interactions with the adsorbent surfaces, making N_2 adsorption more dependent on micropore accessibility and mesopore volume than surface area or specific adsorbent–adsorbate interactions. In contrast, SF_6 possesses high polarizability and a larger size (≈5.15 Å).[46–48] These properties provide stronger interactions with the material surfaces, which explains the adsorption capacity trend: ACM > CS-CO_2 > CS-$ZnCl_2$ > Fe-BTC. The adsorption of SF_6 molecules leads to significant heat generation due to the strong interactions with energetically favorable

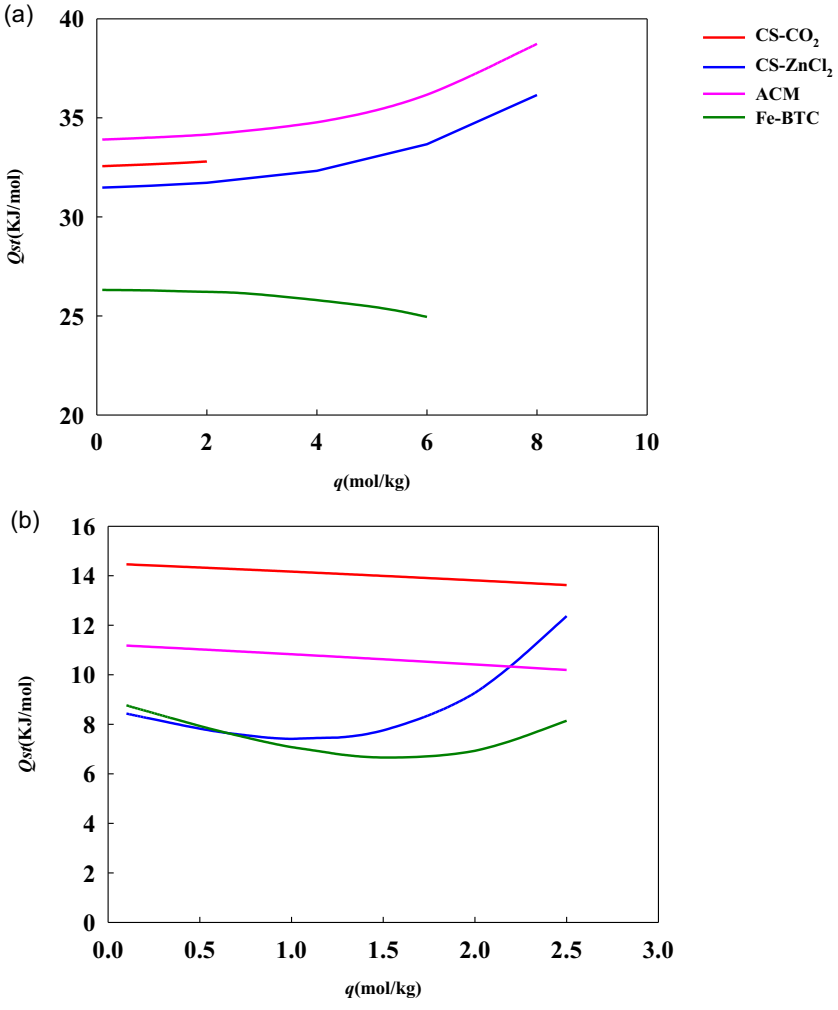

Figure 4. Isosteric heat of adsorption of: a) SF_6 and b) N_2.

adsorption sites located within the pore walls.[60] This results in a linear increase of Q_{st} with increasing uptake. In contrast, N_2 exhibits a linear Q_{st} profile with significantly lower values ranging from 6 to 15 kJ mol^{-1} across all materials (see Figure 4b). This behavior reflects the limited interaction of N_2 with the porous matrices. As N_2 loading increases, the available adsorption sites become saturated, leading to a gradual reduction in adsorption enthalpy and thus a decline in Q_{st}.[61]

In addition, Henry's constants, K_H, are essential for understanding the interactions between the four porous solid matrices (CS-CO_2, CS-$ZnCl_2$, ACM, and Fe-BTC) and the two gases under study (SF_6 and N_2). Both Q_{st} and K_H provide insight into the affinity between the gas molecules and the surface of the adsorbent materials.[52,56,60] Stronger adsorbate–absorbent interactions typically result in higher values of both Q_{st} and K_H. The Henry's constants were calculated using the virial Equation (equation (S7), Supporting Information), with the relevant parameters presented in Table S4, Supporting Information. For the initial screening metric, K_H serves as a key indicator for selecting the most suitable materials for SF_6/N_2 separation and purification processes. For SF_6, the K_H values follow the order: ACM > CS-CO_2 > CS-$ZnCl_2$ > Fe-BTC. In contrast, for N_2, the order is: CS-CO_2 > ACM > CS-$ZnCl_2$ > Fe-BTC (see **Figure 5**). These trends in K_H are consistent with the patterns observed for Q_{st}, further supporting the conclusion that the nature and strength of adsorbate/adsorbent interactions are governed by the structural characteristics of the pores and the presence of energetically favorable adsorption sites. This relationship also accounts for the observed linear dependence of Q_{st} on increasing gas loading.[62–64]

2.3. Selectivity of SF_6/N_2 Mixture Predicted Using IAST Theory

Sulfur hexafluoride (SF_6) is extensively used in the electrical industry as an insulating gas, often blended with nitrogen in concentrations ranging from 0.1 to 50 wt% to mitigate its environmental impact.[13] However, there is currently no standardized method for capturing SF_6 at the end of its life cycle. To evaluate the potential of various porous solid matrices for separating SF_6/N_2 mixtures, the selectivity of each material was assessed based on its preferential adsorption behavior. The Toth model parameters (see Table S3, Supporting Information), determined using the adsorption equilibria of pure SF_6 and N_2, were combined with the IAST to predict the composition of the adsorbed phase in the industrially relevant gas mixture ($y_{SF6} = 0.02$, $y_{N2} = 0.98$, see Figure S5 and Table S5, Supporting Information). The calculated selectivity values, shown in **Figure 6** and Table S6, Supporting Information, indicate that all materials favor SF_6 over N_2, following the trend: ACM > CS-$ZnCl_2$ > Fe-BTC > CS-CO_2. This order correlates with the decreasing surface area of the materials (see Table 1), because larger surface areas and favorable pore structures can accommodate more adsorbate molecules, enhancing SF_6/N_2 separation. Moreover, when a material is selective towards SF_6 and evaluated under dynamic conditions with diluted SF_6/N_2 feeds, the retention of SF_6 in the adsorption column is significantly prolonged, enabling the production of N_2 with purities exceeding 99.999%.[17] These findings are consistent with the working capacity results previously discussed (see Figure 2). An important factor influencing separation is the shape of the adsorption isotherms for each pure component.[65] As shown in Figure S1 and S2, Supporting Information, the SF_6 isotherm exhibits a steeper slope at low pressures, while the N_2 isotherm is more linear. This behavior confirms that SF_6 adsorption is favored, whereas N_2 remains in the gas phase, supporting the observed selectivity results.

To gain a deeper understanding of the dominant factors influencing the separation of the SF_6/N_2 mixture, the results obtained in this study were compared with those reported in the literature under similar conditions (0.1 MPa and temperatures of 298.15 and 303.15 K).[17,19,28–40,43,44,66,67] This comparative analysis focused on key structural properties (surface area (S_{BET}) and total pore volume (v_{total})), along with SF_6 adsorption capacity (q_{SF6}) and selectivity, as presented in **Figure 7** and Table S8 and S9, Supporting Information. The most representative materials in Figure 7a,b include Ph_6M_4Cs11, Mg-MOF-74, CO-MOF-74, $Ph_8M_2Cs_{11}$, $Ph_6M_4Cs_9$, CAK1, CAK2, CAK3, CAK4, PC-800, Kureha carbon, $Ph_8M_2Cs_9$ and ACM (Table S7, Supporting Information). The materials exhibiting the highest adsorption capacity typically possess S_{BET} values in the range of 1500–2000 m^2 g^{-1} and v_{total} values

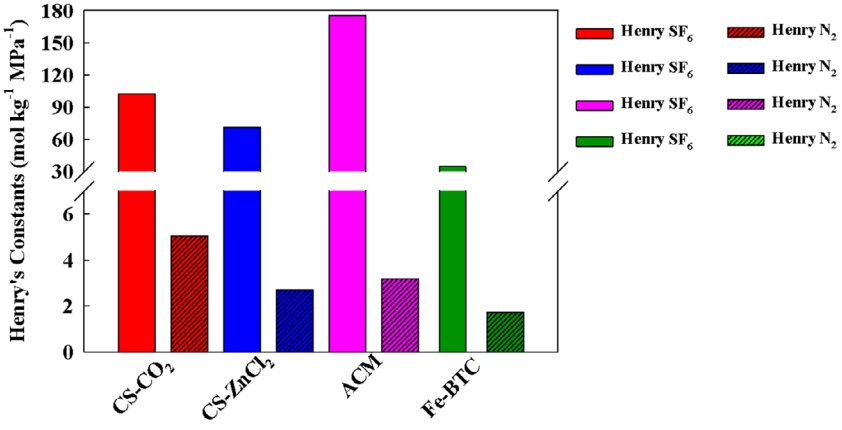

Figure 5. Henry's law constants at 303.15 K.

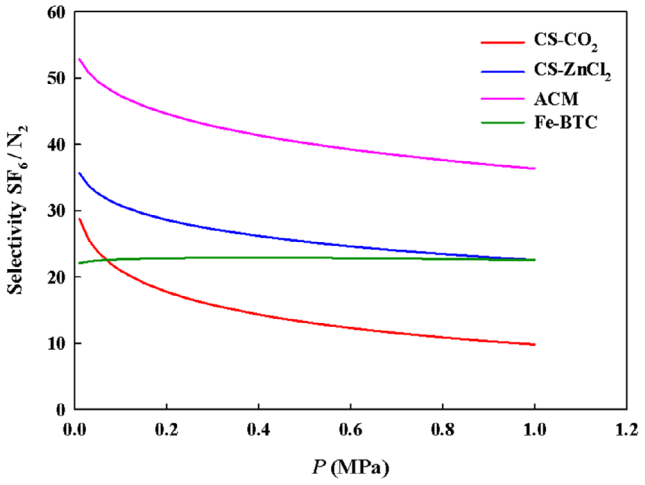

Figure 6. Selectivity of CS-CO_2, CS-$ZnCl_2$, ACM, fe-BTC to SF_6 over N_2 as a function of pressure at 303.15 K for the equilibrium gas phase composition of the SF_6/N_2 mixture ($y_{SF6} = 0.02$ and $y_{N2} = 0.98$).

of ≈0.5–1.1 $cm^3 g^{-1}$. Among them, $Ph_6M_4Cs_{11}$, $Ph_8M_2Cs_{11}$, and $Ph_6M_4Cs_9$ are synthetic ACs derived from phenolic carboxylic resins, melamine, and various heavy metals.[33] Their enhanced adsorption capacity can be attributed to the structural properties developed during chemical activation, which foster large surface areas, high pore volumes, and abundant microporosity. Additionally, larger total pore volumes facilitate the diffusion of gas molecules into micropores, allowing a greater number of molecules to be stored in the structure of the material, increasing their adsorption capacity.[33] The MOFs Mg-MOF-74 and CO-MOF-74 are characterized by their highly porous frameworks and the presence of dense unsaturated metal sites, which facilitate strong interactions with SF_6 molecules, thereby improving adsorption performance.[28] The ACM material studied in this work also performed strongly (highlighted in the demarcated region of Figure 7a,b) alongside several commercial materials such as AC, BIO-AC, and synthetic ACs (CAK1, CAK2, CAK4, PC-800, Kureha carbon, and $Ph_8M_2Cs_9$). These materials are distinguished by their high porosity and elongated micropores, which are significantly influenced by the chemical agents employed during activation.[19,32,33]

As shown in Figure 7c,d, BUT-53 exhibits the highest SF_6/N_2 selectivity, despite not possessing the largest surface area or total pore volume. This outstanding performance is attributed to the presence of optimally sized pores together with aromatic and metal sites,[17] which generate strong supramolecular interactions with SF_6 while reducing the affinity for N_2.[17] These results highlight that selectivity is favored by the functional groups present within the pores, which establish adsorbent–adsorbate interactions that, in combination with structural features, facilitate SF_6 separation. Therefore, an efficient material must balance its selectivity and structural properties to optimize SF_6 capture.[68] In contrast, it is remarkable that ACs such as AC PC-800 and PC-750 demonstrate superior selectivity, a result of their tailored

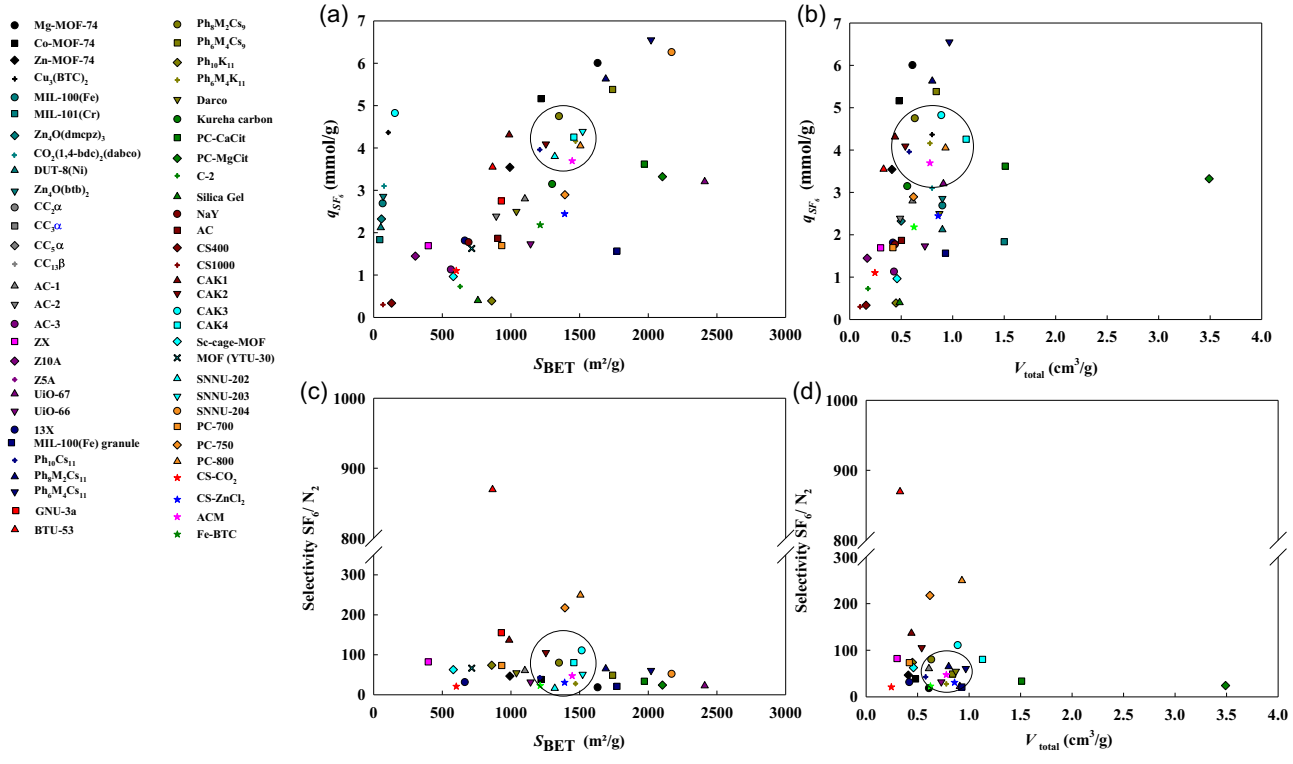

Figure 7. Comparison of materials studied in this work and literature, taking into account: a) q_{SF_6} versus S_{BET}; b) q_{SF_6} versus v_{total}; c) SF_6/N_2 selectivity versus S_{BET}; and d) SF_6/N_2 selectivity versus v_{total} at 303.15 K and 0.1 MPa for the equilibrium gas phase composition of $y_{SF6} = 0.02$ and $y_{N2} = 0.98$.[17,19,28,30,31,33,34,36–38,40,44,66].

microporous structure.[19] The materials investigated in this work also exhibit promising selectivity values. Importantly, they are derived from residual biomass, offering a more sustainable and cost-effective alternative compared to conventional synthetic or commercial materials. Nevertheless, when selecting adsorbents for industrial applications, a range of factors must be considered, including the adsorption capacity for gas mixtures, selectivity, material renderability, adsorption/desorption kinetics, compatibility, regeneration capacity, and overall production cost.

2.4. Criteria for Material Selection

Material selection plays a crucial role in the separation of complex gas mixtures, requiring comparative analysis based on adsorption equilibrium data and selectivity. To identify optimal adsorbents, Yang's and Ackley's FOM metrics are often employed, as they provide a comprehensive evaluation of working capacity, selectivity, and regeneration capacity.[69–71] These performance indicators significantly influence process efficiency, gas purity, and material lifespan.[72] In this study, both metrics were applied to compare the four porous materials developed herein with 36 benchmark materials reported in the literature for the separation of SF_6/N_2 mixture ($y_{SF6} = 0.02$ and $y_{N2} = 0.98$), under the conditions of 0.1 MPa and 303.15 K, with a desorption pressure of 0.001 MPa at the same temperature. The comparative results are summarized in Table S10, Supporting Information and **Figure 8**. According to Ackley's FOM, which focuses on working capacity (see Figure 8), ACM ranks 13th among the evaluated materials, following the order: $Ph_6M_4K_{11}$ > SNNU-204 > $Ph_8M_2Cs_{11}$ > UiO-66 > SNNU-203 > $Ph_6M_4Cs_{11}$ > Zn-MOF-74 > Darco > SNNU-202 > CAK4 > UiO-67 > PC-800 > ACM. These top-performing materials can be broadly classified into three categories: i) MOFs such as SNNU-204, SNNU-203, Zn-MOF-74, and UiO-67; ii) ACs derived from phenolic resins, including $Ph_6M_4K_{11}$, $Ph_8M_2Cs_{11}$, and $Ph_6M_4Cs_{11}$; iii) Commercial and biomass-based ACs, such as Darco, CAK4, PC-800, and ACM.

Despite their high performance, MOFs may pose scalability and cost challenges at an industrial level. Conversely, ACM demonstrates a balance of performance and processability, with favorable structural characteristics—particularly its microporosity—that make it a promising candidate for gas separation applications.

Regarding the Yang's FOM metric (see Figure 8), which relates working capacity to pure component selectivity, the highest-ranking materials were mostly commercial ACs (PC-800, PC-750, CAK1, CAK3, CAK4 and ACM), MOFs (SNNU-204, SNNU-203, Zn-MOF-74, YTU-30-MOF and UiO-66), phenolic resin ACs ($Ph_6M_4K_{11}$, $Ph_8M_2Cs_{11}$), and porous organic cages (CC3α). The performance of the different materials is ordered as follows: PC-800 > SNNU-204 > $Ph_6M_4K_{11}$ > PC-750 > $Ph_8M_2Cs_{11}$ > CAK4 > YTU-30-MOF > CAK1 > UiO-66 > SNNU-203 > CAK3 > CC3α > Zn-MOF-74 > $Ph_6M_4Cs_{11}$ > ACM.

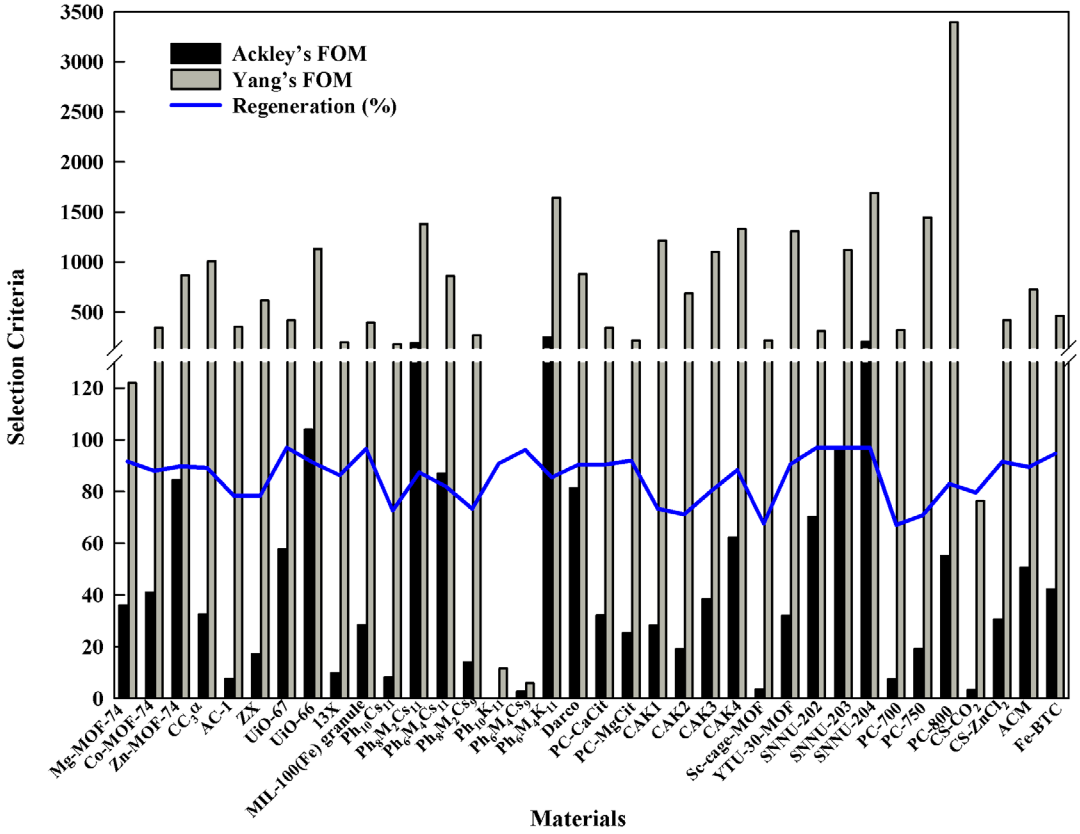

Figure 8. Selection criteria of porous solid matrices using ackey's FOM, Yang's FOM, and regeneration capacity at an adsorption pressure of 0.1 MPa and 303.15 K, with desorption at 0.001 MPa and 303.15 K.

While many of the top performers are ACs, their highly microporous structure, though advantageous for adsorption, may hinder regeneration, thereby increasing operational costs. This trade-off highlights the need for a more targeted approach in adsorbent selection. To this end, the materials were further evaluated under conditions more representative of industrial operation, considering a broader range of pressures and temperatures: **Condition 1:** Feed pressure of 1 MPa at 303.15 K and desorption pressure of 0.1 MPa at 303.15 K. **Condition 2:** Feed pressure of 1 MPa at 303.15 K and desorption pressure of 0.1 MPa at 313.15 K. **Condition 3:** Feed pressure of 1 MPa at 303.15 K and desorption pressure of 0.001 MPa at 323.15 K.

This multi-scenario analysis allows for a more comprehensive evaluation of material performance, particularly in terms of robustness, operational versatility, and industrial applicability.

Under these operating conditions, the limited availability of experimental data in the literature reduces the number of comparable materials. For the first condition, the materials are ranked as follows: Matériaux de l'Institut Lavoisier (MIL)-100(Fe) granulated > Fe-BTC > ACM > CS-ZnC_{l2} > UIO-67 > UIO-66 > 13X > CS-CO_2 (see **Figure 9**a). While most materials exhibit good working capacities, the pore structure strongly influences their regeneration performance. In this scenario, the regeneration efficiency for 13X and CS-CO_2 lies in the range of 20–25%, whereas for the other materials, it is ≈55%. These findings suggest that although a substantial amount of gas is adsorbed, the limited regeneration restricts the materials' overall efficiency and hampers their long-term reusability. Under the second condition, an increase in desorption temperature significantly improves the regeneration: MIL-100(Fe) granulated > Fe-BTC > ACM > CS-$ZnCl_2$ > 13X > CS-CO_2 (see Figure 9b). Here, the regeneration capacity improves to 25–50% for 13X and CS-CO_2 and reaches 90–95% for the other materials, thereby markedly increasing their working capacities. Finally, in the third

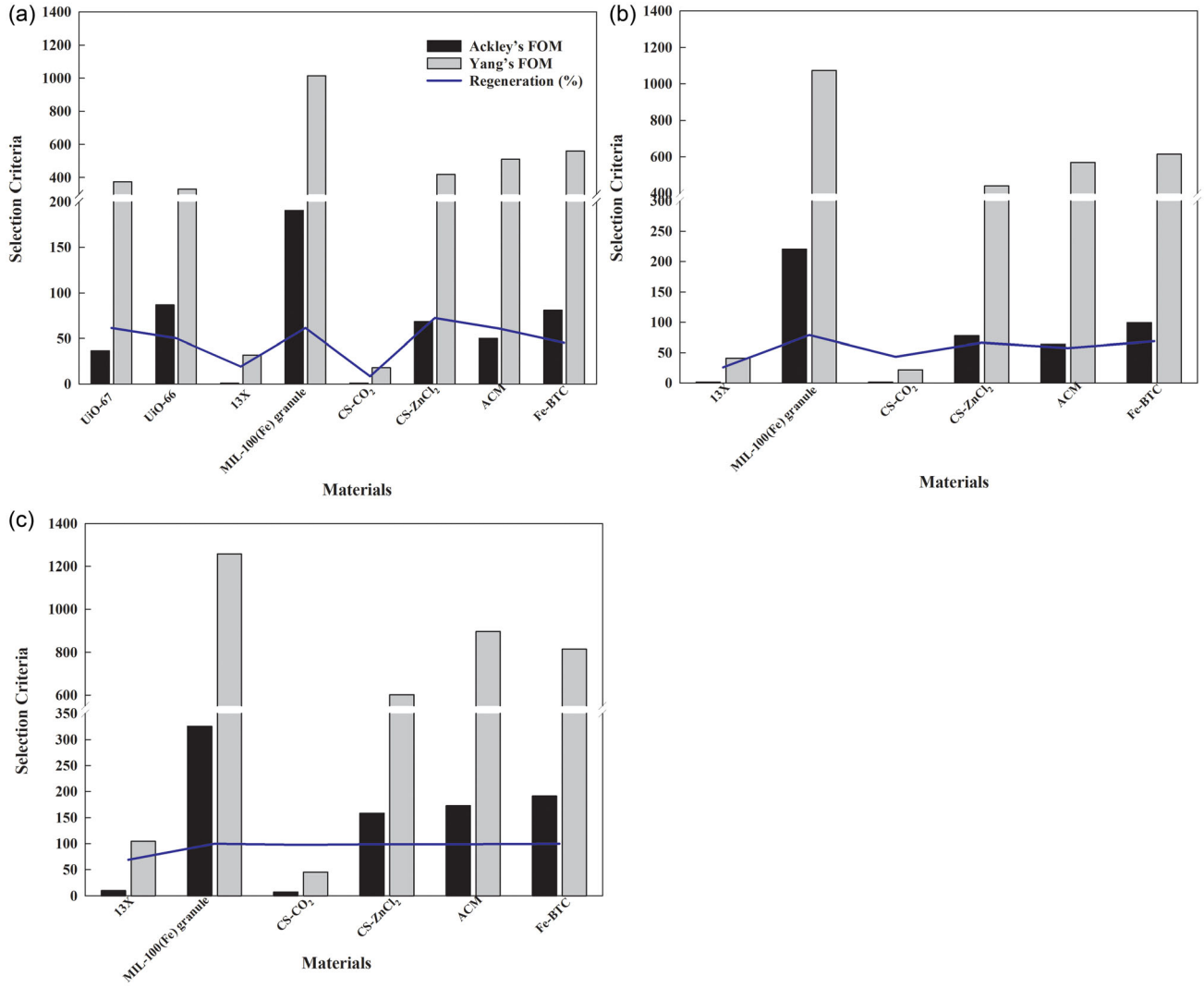

Figure 9. Selection criteria for porous solid matrices using ackey's FOM, and Yang's FOM for: a) condition 1 - feed pressure of 1 MPa at 303.15 K and desorption pressure of 0.1 MPa at 303.15 K, b) Condition 2 - feed pressure of 1 MPa at 303.15 K and desorption pressure of 0.1 MPa at 313.15 K, and c) Condition 3 - feed pressure of 1 MPa at 303.15 K and desorption pressure of 0.001 MPa at 323.15 K.

condition, full regeneration is achieved due to the elevated desorption temperature and lower pressure. The performance order shifts slightly to: MIL-100(Fe) granulated > ACM > Fe-BTC > CS-$ZnCl_2$ > 13X > CS-CO_2 (see Figure 9c). Importantly, ACM exhibits a significant improvement, outperforming Fe-BTC under these harsher desorption conditions. This suggests that ACM's porous architecture supports more efficient desorption at elevated temperatures. Such enhanced regeneration not only increases working capacity but also provides ACM with a clear advantage in terms of stability and long-term operational reusability in gas separation processes.

3. Conclusions

The materials investigated in this study, ACM, CS-$ZnCL_2$, Fe-BTC, and CS-CO_2, demonstrate significant potential for the capture and separation of SF_6 from SF_6/N_2 mixtures, owing to their diverse structural characteristics that enhance SF_6 selectivity. Across the entire pressure range evaluated, SF_6 adsorption is favored in all porous solid matrices due to the well-developed microporosity and high surface areas, which enable efficient gas packing. At high pressures, this structural advantage significantly boosts the adsorption capacity for SF_6. In contrast, N_2 adsorption is more pronounced at low pressures, particularly in CS-CO_2, as evidenced by higher Henry's law constants, indicating stronger interactions at initial loadings. The efficiency of the materials was further assessed through working capacity calculations under varying pressure and temperature conditions. The results underscore the critical role of surface area not only in maximizing capacity but also in improving regeneration and overall separation performance. Additionally, the interplay between selectivity and working capacity was examined, highlighting the importance of achieving a balance between adsorption strength and desorption ease. A comparative analysis with state-of-the-art materials from the literature confirms the competitive performance of the studied materials, particularly ACM, which stands out due to its excellent working capacity and regeneration behavior. ACM exhibits the highest SF_6 adsorption capacity among the materials studied, due to its high surface area, well-distributed pore volume across micro- and mesopores, and favorable polarity of its active sites. This combination enables stronger interactions with SF_6 molecules, explaining its high selectivity over N_2 and its efficiency in SF_6/N_2 separation. The correlation between the diameter of SF_6, the pore distribution of ACM, and its polarity makes this material a particularly promising adsorbent for the SF_6 capture and storage applications. In summary, this work provides valuable insights for the design and optimization of SF_6 capture and separation processes, reinforcing the potential of these materials for pilot-scale implementation. The findings pave the way for the development of cost-effective and efficient solid porous adsorbents for industrial gas separation applications.

Supporting Information

The authors have cited additional references within the Supporting Information.[75–77]

Acknowledgements

The authors acknowledge the financial support from the LIFE-4-F gases project, LIFE20 CCM/ES/001748, funded by the EU LIFE Programme. This work was also financed by national funds from FCT—Fundação para a Ciência e a Tecnologia, I.P., under the scope of the project UID/50006/2023 of the Associate Laboratory for Green Chemistry—LAQV REQUIMTE, grant 2022.11909.BD (J.E.S, DOI: 10.54499/2022.11909.BD), the contracts of Individual Call to Scientific Employment Stimulus 2020.00835.CEECIND (J.M.M.A.) / 2021.01432.CEECIND (A.B.P.) / CEECIND/004431/2022 (I.M.), and the Norma Transitória DL 57/2016 Program Contract (R.P.P.L.R. and M.B.). Finally, the authors acknowledge the results obtained by the Laboratório de Análises—LAQV REQUIMTE.

Wiley and FCT/b-on have an agreement to cover the cost of your open access publishing. Please note: FCT/b-on strongly encourages you to apply a CC BY license to your article as this will amplify the article visibility and knowledge advancement, while retaining full credit of your authorship.

Conflict of Interest

The authors declare no conflict of interest.

Data Availability Statement

The data that support the findings of this study are available from the corresponding author upon reasonable request.

Keywords: adsorption · fluorinated gases · ideal adsorbed solution theory · recovery · separation · sulfur hexafluoride (SF_6)

[1] S. Heikonen, M. Heino, M. Jalava, S. Siebert, D. Viviroli, M. Kummu, *Nat. Food* **2025**, *6*, 331.
[2] European Commission, Consequences of Climate Change https://Climate.ec.europa.eu/Climate-Change/Consequences-Climate-Change_en (accessed: June 2024).
[3] I. of Medicine, in *Global Climate Change and Extreme Weather Events: Understanding the Contributions to Infectious Disease Emergence: Workshop Summary*, The National Academies Press, Washington, DC **2008**.
[4] S. Bolan, L. P. Padhye, T. Jasemizad, M. Govarthanan, N. Karmegam, H. Wijesekara, D. Amarasiri, D. Hou, P. Zhou, B. K. Biswal, R. Balasubramanian, H. Wang, K. H. M. Siddique, J. Rinklebe, M. B. Kirkham, N. Bolan, *Sci. Total Environ.* **2024**, *909*, 168388.
[5] Publications Office of the European Union, https://edgar.jrc.ec.europa.eu/report_2023 (accessed: September 2024).
[6] B. K. Sovacool, S. Griffiths, J. Kim, M. Bazilian, *Renewable Sustainable Energy Rev.* **2021**, *141*, 110759.
[7] X. Fang, X. Hu, G. Janssens-Maenhout, J. Wu, J. Han, S. Su, J. Zhang, J. Hu, *Environ. Sci. Technol.* **2013**, *47*, 3848.
[8] Z. Cui, Y. Li, S. Xiao, S. Tian, J. Tang, Y. Hao, X. Zhang, *Sci. Total Environ.* **2024**, *906*, 167347.
[9] US Environmental Protection Agency | US EPA, *Sulfur Hexafluoride (SF6) Basics*, https://www.epa.gov/eps-partnership/sulfur-hexafluoride-sf6-basics#:~:text=Approximately%2067%25%20of%20all%20SF,to%20reduce%20SF6%20emissions (accessed: August 2025).
[10] M.-B. Kim, K.-M. Kim, T.-H. Kim, *Chem. Eng. J.* **2018**, *339*, 223.
[11] A. Kraut, R. Lilis, *Occup. Environ. Med.* **1990**, *47*, 829.

[12] C. T. Dervos, P. Vassiliou, *J. Air Waste Manage. Assoc.* **2000**, *50*, 137.
[13] E. K. Lee, J. D. Lee, H. J. Lee, B. R. Lee, Y. S. Lee, S. M. Kim, H. O. Park, Y. S. Kim, Y.-D. Park, Y. D. Kim, *Environ. Sci. Technol.* **2009**, *43*, 7723.
[14] US Environmental Protection Agency | US EPA, *State and Regional Regulations Related to SF6 Emissions from Electric Transmission and Distribution*, https://www.google.com/search?q=Epa&rlz=1C1GCEA_enPT1054PT1054&oq=Epa&gs_lcrp=EgZjaHJvbWUyBggAEEUYOTIGCAEQRRg8MgYIAhBFGDwyBggDEEUYPDIGCAQQRRg8MgYIBRBFGDwyBggGEEUYQTIGCAcQRRhB0gEIMTI5MGowajeoAgCwAgA&sourceid=chrome&ie=UTF-8 (accessed: August 2025).
[15] S. Bartos, C. Laush, J. Scharfenberg, R. Kantamaneni, *J. Clean Prod.* **2007**, *15*, 979.
[16] S. Bartos, J. Marks, R. Kantamaneni, C. Laush, *Presented at the 132nd TMS Annual Meeting*, Measured Sf 6 Emissions from Magnesium Die Casting Operations, San Diego, CA, March **2003**.
[17] X. Zhang, Y.-L. Zhao, X.-Y. Li, X. Bai, Q. Chen, J.-R. Li, *J. Am. Chem. Soc.* **2024**, *146*, 19303.
[18] C. Y. Chong, Y. Lee, T.-H. Bae, *Chem. Eng. J.* **2021**, *404*, 126577.
[19] W. Fu, J. Wang, Y. Li, Z. Sui, B. Xiao, X. Xu, *Sep. Purif. Technol.* **2024**, *330*, 125496.
[20] S. Tian, X. Zhang, Y. Cressault, J. Hu, B. Wang, S. Xiao, Y. Li, N. Kabbaj, *AIP Adv.* **2020**, *10*, 050702.
[21] H. R. Dehghanpour, P. Parvin, *Appl. Phys. B* **2010**, *101*, 611.
[22] D. Kashiwagi, A. Takai, T. Takubo, H. Yamada, T. Inoue, K. Nagaoka, Y. Takita, *J. Colloid Interface Sci.* **2009**, *332*, 136.
[23] Y.-S. Son, S.-J. Lee, C. Y. Choi, J.-H. Park, T.-H. Kim, I.-H. Jung, *Radiat. Phys. Chem.* **2016**, *124*, 220.
[24] L. Huang, D. Gu, L. Yang, L. Xia, R. Zhang, H. Hou, *J. Environ. Sci.* **2008**, *20*, 183.
[25] J. Canivet, A. Fateeva, Y. Guo, B. Coasne, D. Farrusseng, *Chem. Soc. Rev.* **2014**, *43*, 5594.
[26] S. Ullah, K. Tan, D. Sensharma, N. Kumar, S. Mukherjee, A. A. Bezrukov, J. Li, M. J. Zaworotko, T. Thonhauser, *Angew. Chem. Int. Ed.* **2022**, *61*, e202206613.
[27] H. and R. I. The Air-Conditioning, *AHRI. (2014). AHRI 700 (SI): Specifications for Refrigerants*, https://www.ahrinet.org (accessed: August 2025).
[28] M.-B. Kim, S.-J. Lee, C. Y. Lee, Y.-S. Bae, *Micropor. Mesopor. Mater.* **2014**, *190*, 356.
[29] I. Senkovska, E. Barea, J. A. R. Navarro, S. Kaskel, *Micropor. Mesopor. Mater.* **2012**, *156*, 115.
[30] T. Hasell, M. Miklitz, A. Stephenson, M. A. Little, S. Y. Chong, R. Clowes, L. J. Chen, D. Holden, G. A. Tribello, K. E. Jelfs, A. I. Cooper, *J. Am. Chem. Soc.* **2016**, *138*, 1653.
[31] W.-S. Cho, K.-H. Lee, H.-J. Chang, W. Huh, H.-H. Kwon, *Korean J. Chem. Eng.* **2011**, *28*, 2196.
[32] W. Zhu, J. C. Groen, F. Kapteijn, J. A. Moulijn, *Langmuir* **2004**, *20*, 5277.
[33] Y. Yang, K. Goh, C. Y. Chuah, H. E. Karahan, Ö. Birer, T.-H. Bae, *Carbon* **2019**, *155*, 56.
[34] R. Sun, C.-W. Tai, M. Strømme, O. Cheung, *ACS Appl. Nano Mater.* **2019**, *2*, 778.
[35] X. Peng, J. M. Vicent-Luna, Q. Jin, *ACS Appl. Mater. Interfaces* **2020**, *12*, 20044.
[36] W. Fu, J. Wang, Y. Li, Z. Sui, X. Xu, *Sep. Purif. Technol.* **2024**, *348*, 127788.
[37] Y.-P. Li, X.-J. Zhang, J.-J. Ni, W.-J. Ji, S. Li, Y.-L. Li, W. Wen, J. Wang, Z.-Y. Sui, X.-F. Xu, *Sep. Purif. Technol.* **2024**, *343*, 126995.
[38] Y.-P. Li, J.-J. Ni, S. Li, J. Wang, Z.-Y. Sui, X.-F. Xu, *J. Solid State Chem.* **2024**, *329*, 124443.
[39] S. Chen, Y. Shen, Z. Guan, B. Liu, Z. Tang, D. Zhang, B. Fu, *J. Chem. Eng. Data* **2020**, *65*, 4044.
[40] S.-M. Li, Q. Zhang, H.-C. Jiang, Q.-L. Ni, L.-C. Gui, X.-J. Wang, T.-L. Hu, *Chem. Eng. J.* **2024**, *496*, 154026.
[41] X. Sun, L. Zhou, J. Chen, Z. Jia, Z. Zhao, Z. Zhao, *J. Mater. Chem. A* **2025**, *13*, 2360.
[42] S.-Q. Yang, T.-L. Hu, B. Chen, *Sci. China Chem.* **2023**, *66*, 2181.
[43] M.-B. Kim, T.-H. Kim, T.-U. Yoon, J. H. Kang, J.-H. Kim, Y.-S. Bae, *J. Ind. Eng. Chem.* **2020**, *84*, 179.
[44] H. Wang, L. Shi, Z. Xiong, S. Ma, H. Cao, S. Cai, Z. Qiao, J. Pan, Z. Chen, *Chem. Commun.* **2024**, *60*, 2397.
[45] J. E. Sosa, R. P. P. L. Ribeiro, I. Matos, M. Bernardo, I. M. Fonseca, J. P. B. Mota, J. M. M. Araújo, A. B. Pereiro, *Int. J. Refrig.* **2025**, *176*, 66.
[46] National Institute of Standards and Technology (NIST), *Experimental Polarizabilites* **2022**, https://cccbdb.nist.gov/pollistx.asp#2015Tha/Wu:144302 (accessed: August 2025).
[47] J. Li, Y. Chen, T. Ke, Y. Jin, R. Fan, G. Xu, L. Yang, Z. Zhang, Z. Bao, Q. Ren, Q. Yang, *Nat. Commun.* **2025**, *16*, 632.
[48] I. Matito-Martos, J. Álvarez-Ossorio, J. J. Gutiérrez-Sevillano, M. Doblaré, A. Martin-Calvo, S. Calero, *Phys. Chem. Chem. Phys.* **2015**, *17*, 18121.
[49] T. Maihom, S. Choomwattana, S. Wannakao, M. Probst, J. Limtrakul, *ChemPhysChem* **2016**, *17*, 3416.
[50] R. P. P. L. Ribeiro, J. P. B. Mota, *J. Phys. Chem. C* **2021**, *125*, 2411.
[51] D. N. D. L. Mendes, A. Gaspar, I. Ferreira, J. P. B. Mota, R. P. P. L. Ribeiro, *Chem. Eng. Res. Des.* **2021**, *174*, 442.
[52] D. W. Siderius, H. W. Hatch, V. K. Shen, *J. Phys. Chem. B* **2022**, *126*, 7999.
[53] D. Ramirez, S. Qi, M. J. Rood, K. J. Hay, *Environ. Sci. Technol.* **2005**, *39*, 5864.
[54] R. P. P. L. Ribeiro, J. Barreto, M. D. G. Xavier, D. Martins, I. A. A. C. Esteves, M. Branco, T. Tirolien, J. P. B. Mota, G. Bonfait, *Micropor. Mesopor. Mater.* **2020**, *298*, 110055.
[55] S. Builes, S. I. Sandler, R. Xiong, *Langmuir* **2013**, *29*, 10416.
[56] L. Sarkisov, *J. Phys. Chem. C* **2012**, *116*, 3025.
[57] Y. Li, H. Yi, X. Tang, F. Li, Q. Yuan, *Chem. Eng. J.* **2013**, *229*, 50.
[58] R. P. P. L. Ribeiro, B. C. R. Camacho, A. Lyubchyk, I. A. A. C. Esteves, F. J. A. L. Cruz, J. P. B. Mota, *Micropor. Mesopor. Mater.* **2016**, *230*, 154.
[59] F. N. Ridha, P. A. Webley, *Sep. Purif. Technol.* **2009**, *67*, 336.
[60] H. Xu, L. Prasetyo, D. D. Do, D. Nicholson, *Chem. Eng. J.* **2020**, *395*, 125035.
[61] A. V. Palodkar, K. Anupam, Z. Roy, B. B. Saha, G. N. Halder, *Heat Mass Transfer* **2017**, *53*, 3155.
[62] J. Liu, M. D. LeVan, *Carbon* **2010**, *48*, 3454.
[63] M. L. Palash, T. H. Rupam, A. Pal, A. Chakraborty, B. B. Saha, R. Wang, *Chem. Eng. J. Adv.* **2021**, *6*, 100086.
[64] J. Jia, Y. Xing, B. Li, Y. Wu, D. Wang, *Sci. Rep.* **2024**, *14*, 24131.
[65] M. M. Majd, V. Kordzadeh-Kermani, V. Ghalandari, A. Askari, M. Sillanpää, *Sci. Total Environ.* **2022**, *812*, 151334.
[66] P.-J. Kim, Y.-W. You, H. Park, J.-S. Chang, Y.-S. Bae, C.-H. Lee, J.-K. Suh, *Chem. Eng. J.* **2015**, *262*, 683.
[67] J. Jagiełło, T. J. Bandosz, K. Putyera, J. A. Schwarz, *J. Chem. Soc. Faraday Trans.* **1995**, *91*, 2929.
[68] J.-R. Li, R. J. Kuppler, H.-C. Zhou, *Chem. Soc. Rev.* **2009**, *38*, 1477.
[69] R. T. Yang, in *Gas Separation by Adsorption Processes* (Ed: R. T. Yang), Butterworth Publishers, MA, USA **1987**, pp. 9–10.
[70] C. Tien, in *Introduction to Adsorption*, Elsevier, Oxford, UK **2019**.
[71] F. Rouquerol, J. Rouquerol, K. S. W. Sing, P. Llewellyn, G. Maurin, in *Adsorption by Powders and Porous Solids*, 2nd ed., Elsevier, Oxford, UK **2014**, pp. 13–14.
[72] R. P. P. L. Ribeiro, J. E. Sosa, J. M. M. Araújo, A. B. Pereiro, J. P. B. Mota, *Int. J. Refrig.* **2023**, *150*, 253.
[73] J. E. Sosa, R. P. P. L. Ribeiro, I. Matos, M. Bernardo, I. M. Fonseca, J. P. B. Mota, J. M. M. Araújo, A. B. Pereiro, *Int. J. Refrig.* **2025**, *176*, 66.

Manuscript received: June 2, 2025
Revised manuscript received: September 5, 2025
Version of record online: October 8, 2025